Scanning Microscopy Vol. 11, 1997 (Pages 53-66) 0891-7035/97$5.00+.25
Scanning Microscopy International, Chicago (AMF O'Hare), IL 60666 USA

GEOMETRIC PHASE ANALYSIS OF HIGH RESOLUTION ELECTRON MICROSCOPE IMAGES

M.J. Hÿtch

Centre d'Etudes de Chimie Métallurgique, Centre National de Recherche Scientifique, Vitry-sur-Seine, France

Abstract

A new method is described for analysing high resolution lattice fringe images. The image is considered to be composed of a reduced set of major image periodicities. Each periodicity has an associated Fourier component which is allowed to vary as a function of position. It is shown that the local amplitude and geometric phase of lattice fringes can be determined in this way by filtering in Fourier space. A direct relationship is then established between the phase and the displacement of lattice fringes, and between the gradient of the phase and the local reciprocal lattice vector. Examples are given illustrating the use of the phase images for analysing variations in structure from high resolution images. The errors in the amplitude and phase measurement induced by noise are estimated and the circumstances under which the lattice fringe positions correspond to atomic plane positions are outlined.

Key Words: Fourier filtering, image analysis, lattice distortions, deformation measurement, electron microscopy.

*Address for correspondence:
M.J. Hÿtch
Centre d'Etudes de Chimie Métallurgique
Centre National de Recherche Scientifique
15 rue G. Urbain, 94407 Vitry-sur-Seine, France
Telephone number: +33-1-46873593
FAX number: +33-1-46750433
E-mail: hytch@glvt-cnrs.fr

Introduction

A high resolution electron microscope image of a crystal can be considered as a sum of several sets of lattice fringes. The Fourier transform of the image shows which periodicities are present and each Fourier component has an amplitude and phase giving the strength and position of the lattice fringes. For a perfect crystal these will limit themselves to a reduced set of periodicities corresponding to the Bragg reflections.

A high resolution image is never perfect, however, whether this be due to changes in the imaging conditions across the field of view or because the specimen is not perfectly uniform. Indeed, it is these variations which are usually of interest and not the perfect crystal structure, which is often known. If we now take a Fourier transform of the image, then the Bragg spots will still be present but with associated diffuse intensity corresponding to the variations in the structure. Such diffuse intensity in a diffraction pattern can be interpreted in terms of grain size, strain fields, defects etc. However, we have lost the real-space information. For example, where are the defects, how are they distributed, what shape do the grains have? To answer these questions we have devised a way of showing the deviations from a perfect lattice fringe image in real-space.

We shall be showing, in particular, how the variation in the positions of lattice fringes can be imaged. There is, in fact, a renewed interest in using this information in high resolution electron microscopy. It was shown some time ago that rigid body displacements across grain boundaries can be measured to very high accuracy simply by measuring the relative displacements of fringes in an image [25], a methodology which has been developed and expanded more recently [3]. Lattice fringe images of strained multilayers have also been analysed to determine compositional variations [1, 2, 16]. Moiré images, produced either by a crystal superimposed on the specimen [18] or by a grid inserted at the level of the projector lenses [7], have been shown to be useful in obtaining long range information about crystal distortions. Finally, it has recently proposed that the phase information in electron holograms can be used to determine displacement fields in the specimen [22]. The method of geometric phase analysis described here

has been previously used to study images of nanocrystals [12], strained multilayers [10] and antiphase boundaries in [13].

Image Decomposition

We shall begin with a perfect crystal and assume that the image is made up of a reduced set of image periodicities, corresponding to the Bragg spots in the Fourier transform. If I(**r**) is the intensity in the image at position **r** then:

$$I(\vec{r}) = \sum_g H_g \exp\{2\pi i\vec{g} \bullet \vec{r}\} \quad (1)$$

where H_g is the Fourier component for the Bragg periodicity $\vec{g}$. Since H_g is in general complex we can define its amplitude and phase as being A_g and P_g. Variations in the crystal structure can now be introduced by allowing these Bragg periodicities to vary across the image in real-space, both in amplitude and phase [9].

The expression for the image intensity, $I(\vec{r})$, now becomes:

$$I(\vec{r}) = \sum_g H_g(\vec{r})\exp\{2\pi i\vec{g} \bullet \vec{r}\} \quad (2)$$

where

$$H_g(\vec{r}) = A_g(\vec{r})\exp\{i P_g(\vec{r})\} \quad (3)$$

In reciprocal space the equivalent expression is the following:

$$\tilde{I}(\vec{k}) = \sum_g \tilde{H}_g(\vec{k} - \vec{g}) \quad (4)$$

Each Bragg spot in the Fourier transform can therefore be considered as being convoluted with a function $\tilde{H}_g(\vec{k})$. For any particular image the choice of $\tilde{H}_g(\vec{k})$ is not unique so we will define $\tilde{H}_g(\vec{k})$ to be zero for reciprocal vectors $\vec{k}$ beyond the first Brillouin zone. In this way we divide the information in reciprocal space into each Brillouin zone and are sure that no information is excluded from the transformation. The image can now be studied in terms of the set of images $\tilde{H}_g(\vec{k})$.

Bragg filtering

In order to explain the usefulness of representing the image in terms of the set of images $H_g(\vec{r})$ we shall relate the above derivation to ordinary Bragg filtering. An image can be filtered by placing a mask around the spots $\pm\vec{g}$ in the Fourier transform and back-Fourier transforming. From Equation (2) the resulting image will have an intensity distribution $B_g(\vec{r})$ given by:

$$B_g(\vec{r}) = H_g(\vec{r})\exp\{2\pi i\vec{g} \bullet \vec{r}\} + H_{-g}(\vec{r})\exp\{-2\pi i\vec{g} \bullet \vec{r}\} \quad (5)$$

It is easy to show that for a real image, $I(\vec{r})$:

$$H_g(\vec{r}) = H^*_{-g}(\vec{r}) \quad (6)$$

and therefore Equation (5) becomes:

$$B_g(\vec{r}) = 2\Re e[H_g(\vec{r})\exp\{2\pi i\vec{g} \bullet \vec{r}\}] \quad (7)$$

where $\Re e$ denotes the real part. Writing $H_g(\vec{r})$ in terms of amplitude and phase, using Equation (3), we obtain the following result:

$$B_g(\vec{r}) = 2A_g(\vec{r})\cos\{2\pi\vec{g} \bullet \vec{r} + P_g(\vec{r})\} \quad (8)$$

This equation was the starting point for the description of the method of geometric phase analysis described elsewhere for the study of images of nanocrystals [12]. By calculating $H_g(\vec{r})$ we can therefore obtain an image of the amplitude and an image of the phase of the set of lattice fringes as a function of position. Amplitude images show how the strength of a set of fringes $\vec{g}$ varies across an image and can be related to variations in, for example, the thickness of a crystal, the composition or local orientation. They are the HREM (high resolution electron microscopy) analogue to dark-field images in conventional TEM (transmission electron microscopy) and much the same effects need to be considered in order to interpret them. There are important differences too, for example the fact that even in the case of linear interference the fringes in an image result from the 000, $\vec{g}$ and $\vec{g}$- beams whereas in conventional dark-field a single beam is imaged. In this paper however we shall be mostly concerned with the geometric phase images which are more directly interpretable in terms of the specimen structure.

Geometric Phase

The phase images show how regular a set of fringes is across a given image, that is, how even the spacing is between fringes and how the fringes vary from their ideal positions. For an ideal set of fringes, the amplitude and phase will no longer be a function of position and we can write that:

$$B_g(\vec{r}) = 2A_g\cos\{2\pi\vec{g} \bullet \vec{r} + P_g\} \quad (9)$$

In the presence of a displacement field $\vec{g}$, the Bragg fringes of Equation (9) can be rewritten as:

$$B_g(\vec{r}) = 2A_g\cos\{2\pi\vec{g} \bullet \vec{r} - 2\pi\vec{g} \bullet \vec{u}\} \quad (10)$$

from which, by comparison with Equation (8), we obtain that:

$$P_g(\vec{r}) = -2\pi\vec{g} \bullet \vec{u} \quad (11)$$

In this way the phase directly measures the component of the displacement field, u_g, for each set of lattice

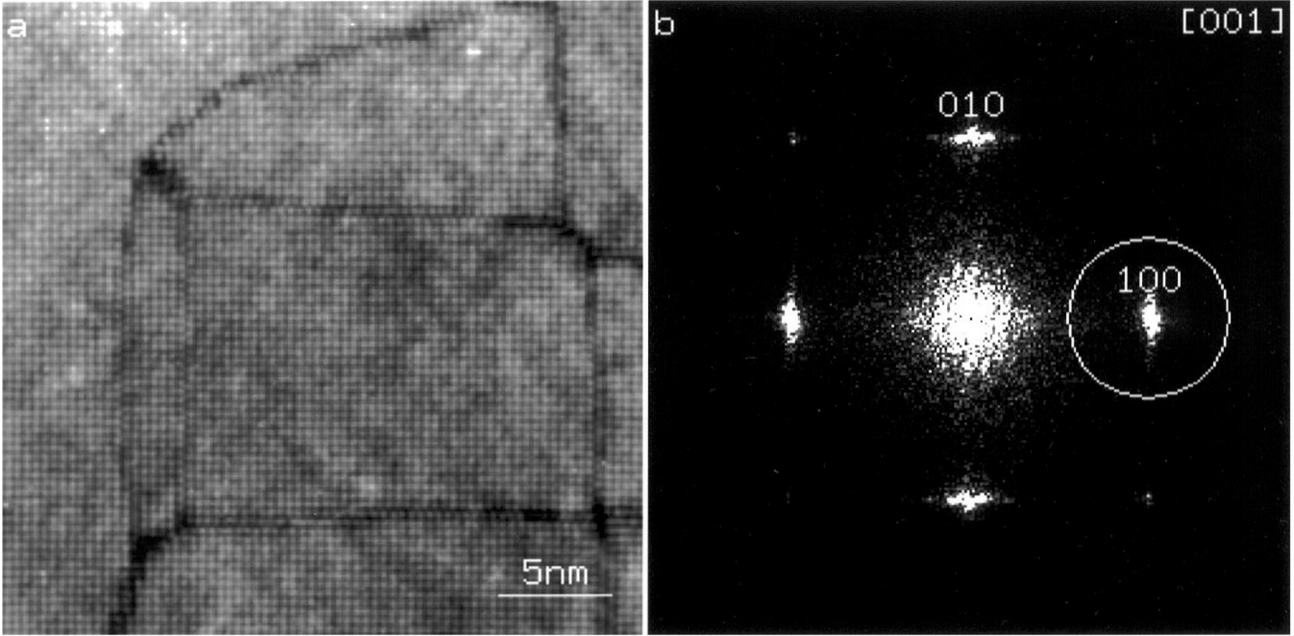

Figure 1. Antiphase domains in long-range ordered Cu_3Au: (**a**) HREM image in [001] projection with objective aperture excluding the {200} spots (courtesy of Laurence Potez); (**b**) diffractogram of HREM image showing the {100} order spots and mask used for 100 filtering.

planes, $\vec{g}$. Combining the results for each lattice plane will give the vectorial displacement field. The representation of displacements in terms of a phase change is analogous to that appearing in the kinematical scattering theory of defects [8].

On the other hand, if the reciprocal vector, $\vec{g}$, for a set of lattice fringes changes by a small amount $\Delta\vec{g}$ then Equation (9) for the lattice fringes becomes:

$$B_g(\vec{r}\,) = 2\,A_g \cos\{2\pi\vec{g} \bullet \vec{r} + 2\pi\Delta\vec{g} \bullet \vec{r}\,\} \quad (12)$$

Comparing this equation with Equation (8) we find that:

$$P_g(\vec{r}\,) = 2\pi\Delta\vec{g} \bullet \vec{r} \quad (13)$$

In a region where the lattice spacing is slightly different, due for example to a change in the lattice parameter, the phase will have a uniform slope corresponding to the difference. The greater the difference in the lattice spacing, the steeper the slope. Mathematically, we can see that the gradient, $\vec{\nabla}P_g$, is given by:

$$\vec{\nabla}P_g = 2\pi\Delta\vec{g} \quad (14)$$

This equation allows us to measure local departures from the average reciprocal lattice vector directly from the phase. The relation is vectorial, so a rotation of the lattice would also be revealed in a phase image and $\Delta\vec{g}$ would be perpendicular to $\vec{g}$. Equation (14) could have been derived directly from Equation (11) as the gradient of the displacement field gives the local lattice parameter.

Holographic reconstruction

The images $H_g(\vec{r})$ can be obtained from the original image in exactly the same way as a single side-band holographic reconstruction except that the reference beam is the $\vec{g}$ periodicity (and with no correction of the objective lens aberrations, see for example [17]). The reason that the phase images are called *geometric* is to distinguish between the positions of fringes in the image (determined by this method) and the actual phase of the beams emerging from the crystal (determined by holography).

The coordinates of $\vec{g}$ are found from the power spectrum of the image, the centre of mass of the intensity in the peak is generally a good method for obtaining sub-pixel accuracy. A mask is placed around the position $\vec{g}$ in the Fourier transform of the image and the back-Fourier transform performed. If necessary, in order to reduce the noise in the final image, the mask can be smaller than the Brioullin zone though the resolution will be reduced. The resulting image $H'_g(\vec{r})$ will be:

$$H_g{'}(\vec{r}\,) = H_g(\vec{r}\,)\exp\{2\pi i\vec{g} \bullet \vec{r}\,\} \quad (15)$$

where

$$2\Re e[H_g'(\vec{r}\,)] = B_g(\vec{r}\,) \quad (16)$$

$$\text{Mod}\,[H_g'(\vec{r}\,)] = A_g(\vec{r}\,) \quad (17)$$

$$Phase\,[H_g'(\vec{r}\,)] = P_g(\vec{r}\,) + 2\pi\vec{g}\bullet\vec{r} \quad (18)$$

The phase image $P_g(\bar{r})$ is obtained by simple subtraction of the phase ramp $2\pi\vec{g}.\bar{r}$ (followed by a renormalisation of the phase between $\pm\pi$) which avoids problems associated with $\vec{g}$ lying between pixels in the digital transform [24].

Examples of Phase Images

Antiphase boundaries

The first example of the use of the method of geometric phase analysis is taken from a study of antiphase boundaries in Cu_3Au [13]. The original image is shown in Figure 1a taken in [001] projection on a JEOL 4000FX operating at 400kV. An objective aperture was used to exclude the {200} reflections thus making the visualisation of the antiphase boundaries easier [20]. The digitisation of the negatives was carried out using a CCD (charge-coupled device) video camera mounted above a light box and all the image processing presented in this paper was carried out using routines within the software package SEMPER (Synoptics, Cambridge, UK) [21].

The atoms in Cu_3Au form a face centred cubic lattice and in the long-range ordered form (as we have here) the atoms of Au are positioned at the corners of the unit cell. Looking in [001] projection the {100} planes are alternatively of pure Cu or rich in Au. Forming an image with only the {100} and {110} spots therefore reveals the positions of the Au rich planes (or the Cu planes depending on the thickness and defocus). Given the symmetry of the unit cell there are four equivalent positions for the origin of the Au sublattice and so translation domains are formed where the Au rich planes are all translated with respect to a neighbouring domain.

This can be seen in the image (Fig. 1a) where across an antiphase boundary the 100 and/or 010 fringes are shifted by half a fringe spacing. By Bragg filtering the original image using the mask shown in Figure 1b the antiphase boundaries for the 100 planes can be seen (Fig. 2a) and similarly for the 010 fringes (Fig. 2b). The amplitude images are similar to dark-field images using the corresponding spot in the diffraction pattern: black lines are seen at the antiphase boundaries (see Figs. 2c and 2d). It is, however, the phase images (Figs. 2e and 2f) which reveal the translation domain structure directly. Because the fringes are translated by half a lattice plane from domain to domain the phase changes by π. In one domain the phase will have a certain constant value and in the neighbouring domain the phase will be shifted by π. In this way the domains show up light or dark in the phase image. The 100 phase gives the component of the translation vector in the 100 direction and the 010 phase in the 010 direction. The results can therefore be combined to give a map of the translation domain structure (Fig. 3). Such an image with four grey levels corresponding to the four translation domains was obtained by adding half the 010 phase to the 100 phase image.

Figure 2 (*on facing page*). Bragg filtered, amplitude and phase images of antiphase domains: (**a**) 100 Bragg filtered image, $B_{100}(\mathbf{r})$; (**b**) 010 Bragg filtered image, $B_{010}(\mathbf{r})$; (**c**) 100 amplitude image, $A_{100}(\bar{r})$; (**d**) 010 amplitude image, $A_{010}(\bar{r})$; (**e**) 100 phase image, $P_{100}(\bar{r})$; (**f**) 010 phase image, $P_{010}(\bar{r})$, black=$-\pi$ white=π. The difference in grey levels corresponds to a change of π in the phase.

Displacement fields around dislocations in silicon

The previous example showed how changing the absolute value of the phase moves the fringes in the image. The next example shows how a displacement field can produce a continuous variation in the phase. Figure 4a shows a high resolution image of a $\Sigma 3$ boundary in silicon taken at 200 kV on a JEOL 200CX along [01] (courtesy of Jean-Luc Putaux). It is not the boundary itself which is of interest here but the edge dislocation located at the step in the centre of the image. The Bragg filtered image using the mask shown in the inset shows the presence of the additional plane (Fig. 4b) but the displacement field is not directly measurable. For this we need the 111 phase image (Fig. 4c).

According to simple elastic theory the component, u_g, of the displacement field parallel to the Burgers vector for the lattice planes, $\vec{g}$, around an edge dislocation is given by:

$$u_g = \frac{2\pi}{d_g}\left(\theta + \frac{\sin 2\theta}{4(1-\nu)}\right) \quad (19)$$

where d_g is the spacing of the planes, θ the angle with respect to the dislocation core in cylindrical coordinates, and ν the Poisson constant for the material [6]. In this projection the 111 fringes are perpendicular to $\vec{b}$ and therefore using Equation (11) we can see that:

$$P_{111}(\vec{r}\,) = -2\pi\,\vec{g}_{111}\bullet\vec{u} \quad (20)$$

$$= -\frac{2\pi}{d_{111}}u_{111} \quad (21)$$

since $g_{111}=1/d_{111}$. In the example shown, $b_{111}=d_{111}$ and by substituting u_{111} from Equation (19) into Equation (21) the following result can be obtained:

$$P_{111}(\vec{r}\,) = -\theta - \frac{\sin 2\theta}{4(1-\nu)} \quad (22)$$

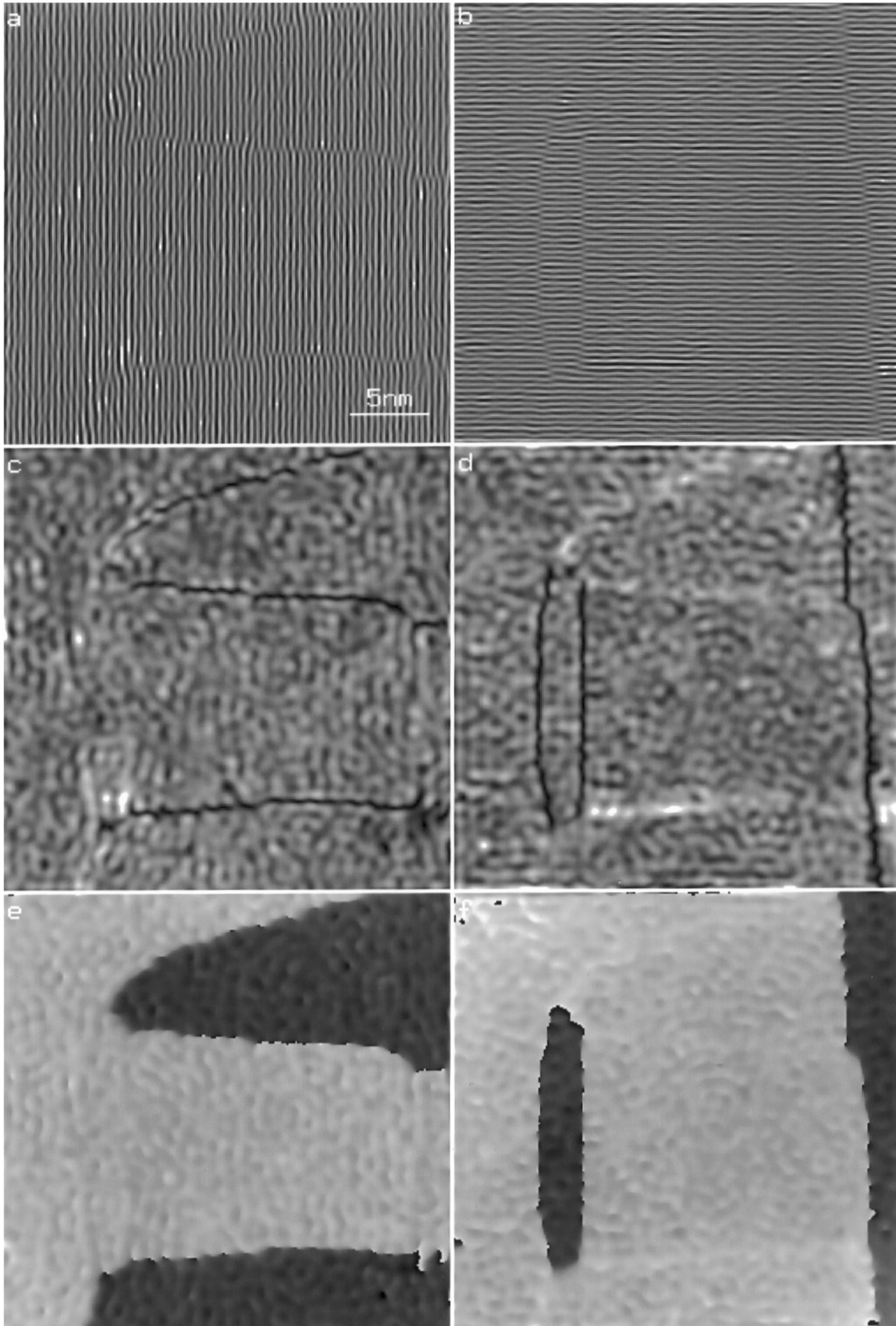
a
b
5nm
c
d
e
f

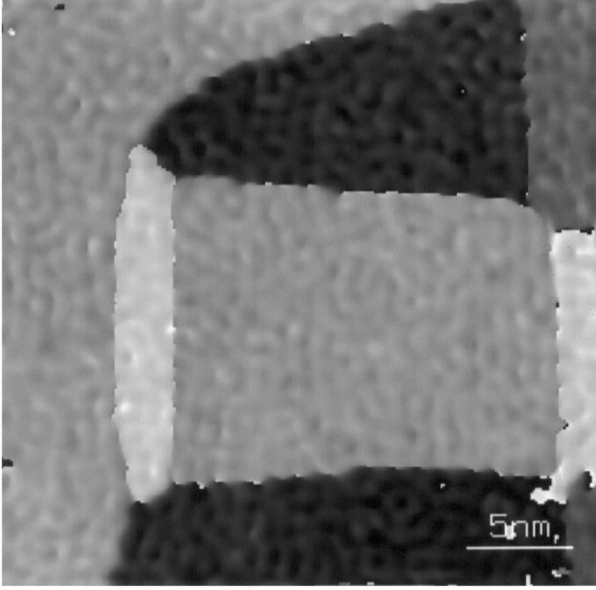

Figure 3. Translation domain structure. The four grey levels correspond to a particular translation domain. Image was calculated using the formula $P_{100}(\bar{r})+1/2\ P_{010}(\bar{r})$.

The phase image therefore has a discontinuity at the dislocation core and elsewhere varies linearly with the angle θ, to a first approximation, given that the second term is much smaller than the first. This point discontinuity, seen in the phase image (Fig. 4c) should not be confused with the discontinuous line where the phase changes abruptly from –π (black) to π (white). The latter is the result of normalising the phase between these two values and should not be interpreted as a discontinuity in the structure. For example, adding a constant phase to the image would change the location of the transition. To reveal the second term in Equation (22) the first term has been removed from the phase image by adding θ to $P_{111}(\bar{r})$ as shown in Figure 4d. Measuring *v* from this image gives a value of 0.3±0.1 which is not surprising but nevertheless gives an independent indication of the validity of the interpretation of the phase in terms of displacement fields.

The appearance of a discontinuity in the phase at a dislocation core can be understood in another way. The component of the Burgers vector, $\bar{b}$, for a set of planes $\bar{g}$ obeys the following relation:

$$\int_L \vec{\Delta} u_g . \vec{dl} = b_g \tag{23}$$

where $\vec{d}l$ is a segment on the loop L containing the dislocation [6]. Using Equation (11) we find that:

$$\int_L \vec{\Delta} P_g . \vec{dl} = 2n\pi \tag{24}$$

where n is the number of extra planes and $b_g = nd_g$. The left hand side of the equation can only be non-zero in the presence of discontinuities and hence a discontinuity must be present at the dislocation core. In this case integrating the 111 phase gradient around the discontinuity gives 2π and hence a single addition plane is present. The next example shows that fractional Burgers vectors can also be detected and measured using the phase.

Figure 5a shows the high resolution image of a dissociated dislocation in silicon. Taking the same set of 111 planes as before, the phase image can be produced (Fig. 5b). Here we see that the global Burgers vector is the same because integrating around a closed loop described in Equation (24) gives 2π. We can remove the associated displacement field by subtracting θ (the angle with respect to dislocation core) from the phase image (Fig. 6a). The dissociated dislocation is now represented by a line discontinuity in the phase. This is shown more clearly by extracting a section across the dislocation (Fig. 6b) and then taking the average line profile (Fig. 6c). The discontinuity is measured from the height of the step in the phase at the mid-point according to Equation (21) and gives a relative displacement of the fringes of 0.64±0.04 111 planes (equivalent to 0.20±0.01 nm). The error is due to the uncertainty with which the phase can be extrapolated in the vicinity of the discontinuity. This result is in accordance with the expected value of n of 2/3, or –1/3. In exactly the same way rigid body displacements across grain boundaries can be measured using this technique [11].

Carbon nanotubes

An illustration of the use of the phase images to measure changes in the reciprocal lattice vector can be found in the next example taken from a study of carbon nanotubes. Figure 7a shows a high resolution image of a multi-shell carbon nanotube taken on a TOPCON 002B microscope (TOPCON, Paramus, NJ) operating at 200kV (courtesy of Pulickel Ajayan). The image corresponds closely to a slice through the structure, the horizontal fringes marking the outer edges of the individual cylinders of graphene [15]. The phase image shown in Figure 7b was formed using the mask marked in the inset. At first sight the 0002 fringes seem quite regular with the phase remaining constant the full length of the tube. Indeed, the phase does remain almost constant across the tube but *along* the tube there is a significant variation, as shown by the averaged phase profile also marked on Figure 8b. The phase forms an approximately v-shape pattern with a constant slope on the left and the right, abruptly changing from one value to the other at the middle. The gradient of the phase is perpendicular to the lattice vector $\bar{g}_{0002}$ which means that the changes are due to a rotation of the lattice. Using Equation (14) we can measure Δg_{0002} and hence the rotation which in this case is 1.4±0.1°.

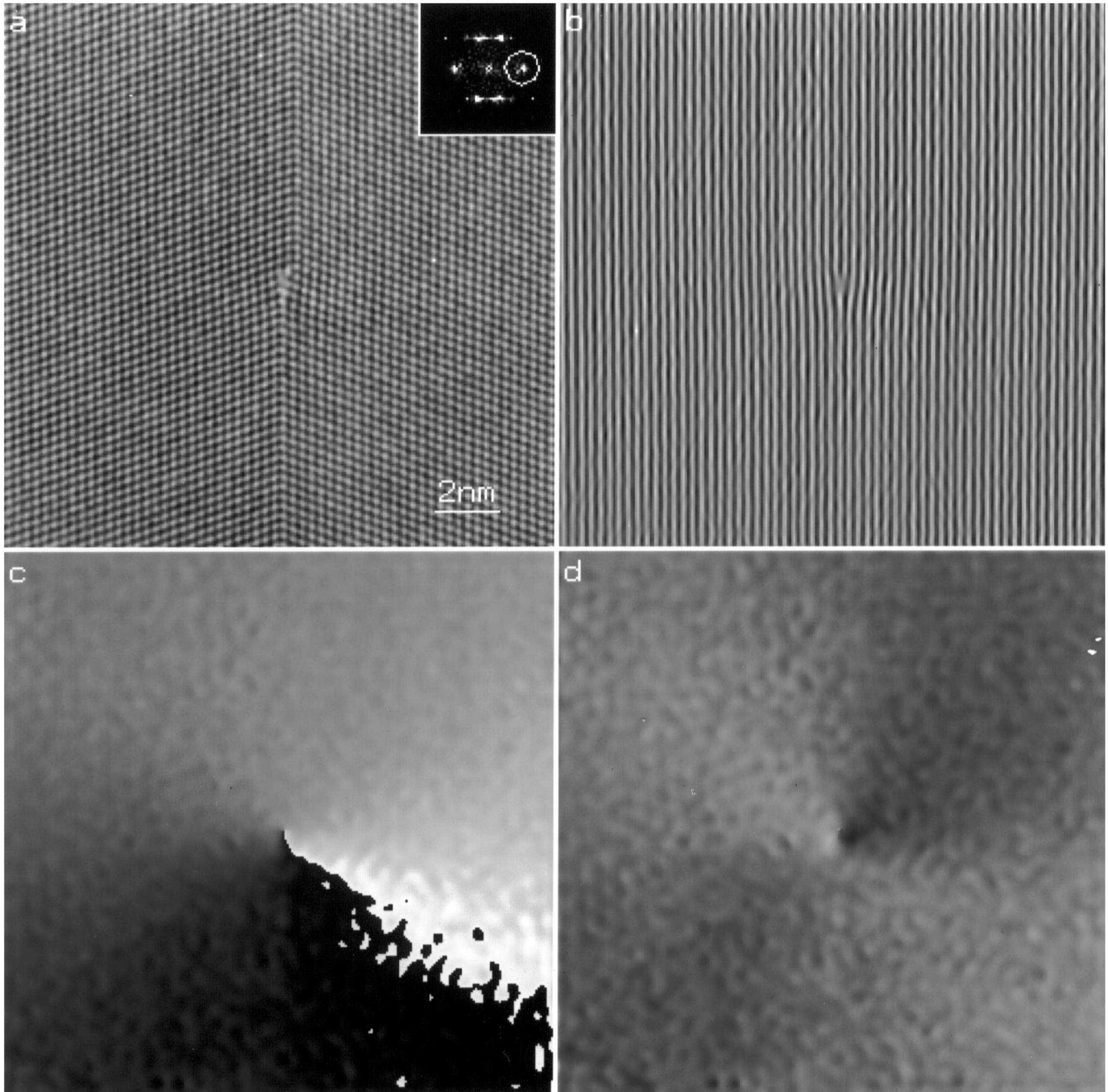

Figure 4. Displacement field around an edge dislocation in silicon: (**a**) HREM image in [01] projection of a Σ3 boundary with associated dislocation (courtesy of Jean-Luc Putaux) diffractogram and 111 mask shown in inset; (**b**) 111 Bragg filtered image, $B_{111}(\bar{r})$; (**c**) 111 phase image, $P_{111}(\bar{r})$, black=–π white=π; (**d**) modified 111 phase image, $P_{111}+\theta$, thus revealing the sin 2θ term in Equation (22), black=–π/4 white=π/4.

The advantage of the phase images over the use of selected area diffractograms is that the accuracy of the measure is easy to calculate and comes directly from the measurement of the gradient of a line. The other advantage is that we can see that the tube is rigidly bent in the middle; the tube is not bend continuously as might have been the case.

Accuracy, Noise and Systematic Errors

The question of accuracy is two-fold. There is the accuracy with which lattice fringe positions are measured from an image using the geometric phase images and there

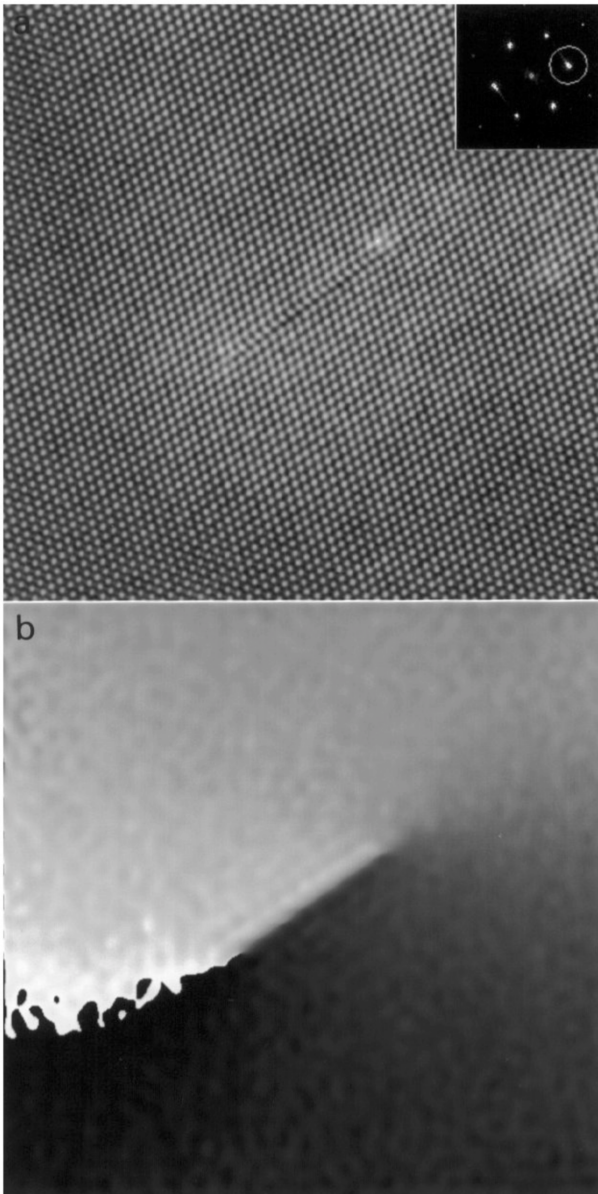

Figure 5. Dissociated dislocation in silicon: (**a**) HREM image in [01] projection (courtesy of Jean-Luc Putaux) diffractogram and 111 mask shown in inset; (**b**) 111 phase image, $P_{111}(\bar{r})$, black=–π white=π.

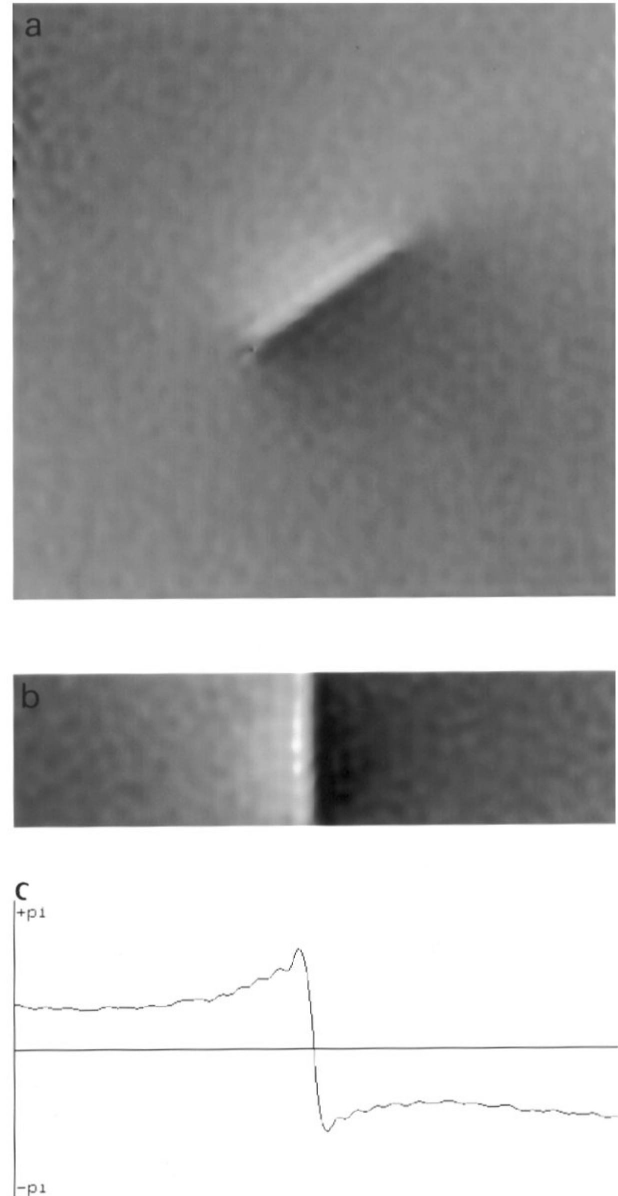

Figure 6. Displacement field due to stacking fault: (**a**) 111 phase image after removal of displacement field due to global Burgers vector; (**b**) section of 111 phase across stacking fault, black=–2π/3 white=2π/3; (**c**) line profile of 111 phase across stacking fault. Discontinuity in the phase of approximately 4π/3 indicates a value of n of 2/3.

is the accuracy with which the lattice fringe positions correspond to the atomic plane positions in the specimen.

Measurement of fringe positions

The effect of noise on lattice fringe positions can be estimated using a simple argument (see Figure 8a for a schematic representation). The complex number $H_g(\bar{r})$ is the signal we are trying to measure in the presence of a noise $n_g(\bar{r})$. In general the noise vector will be pointing in a random direction and can be added to the vector $H_g(\bar{r})$ to produce the measured value. We can see from the diagram that the error in the amplitude $\Delta A_g(\bar{r})$ and the phase $\Delta P_g(\bar{r})$ will both be given approximately by the signal to noise ratio. The error in the lattice plane position Δu_g is more meaningfully expressed as a fraction of the lattice spacing

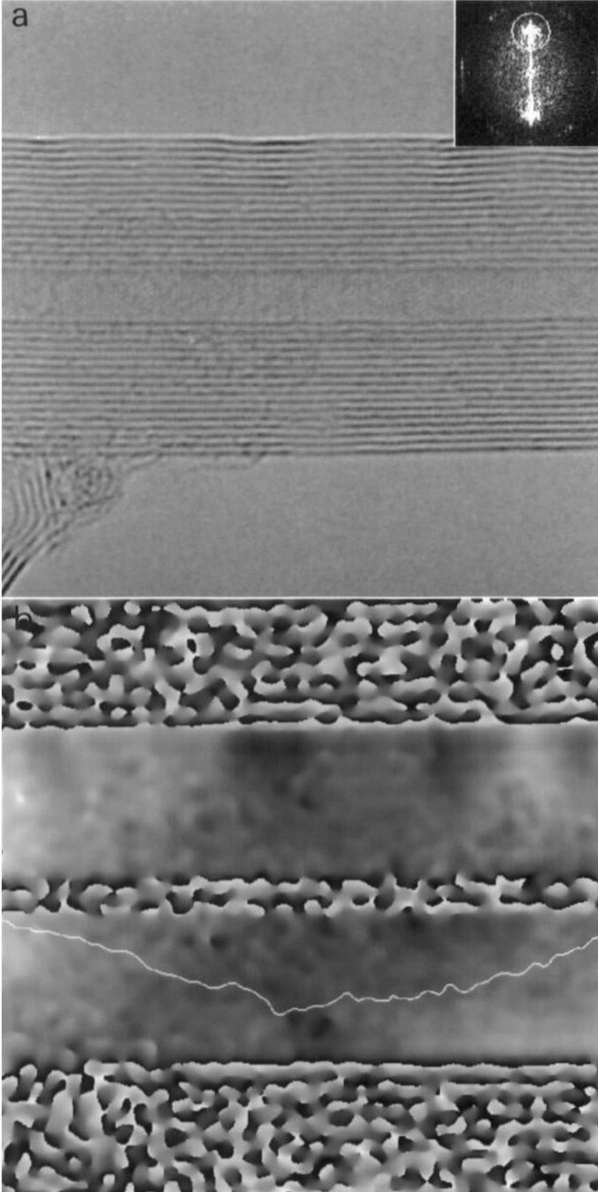

Figure 7. Bending of carbon nanotubes: (**a**) HREM image of multi-shell carbon nanotube (courtesy of Pulickel Ajayan) diffractogram and 0002 mask shown in inset; (**b**) 0002 phase image, $P_{0002}(\bar{r})$, and average phase profile shown as line trace. Change in gradient of the phase gives the rigid rotation to be 1.4±0.1°.

d_g so summarizing the results gives the following estimates:

$$\Delta A_g(\vec{r}) \simeq \left|\frac{noise}{signal}\right| \qquad (25)$$

$$\Delta P_g(\vec{r}) \simeq \left|\frac{noise}{signal}\right| \qquad (26)$$

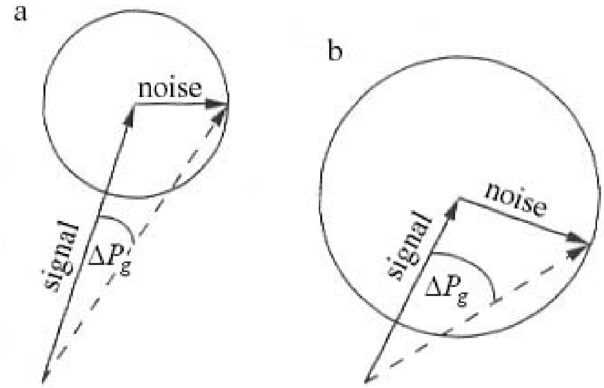

Figure 8. Schematic diagram illustrating the effect of noise which produces an error ΔP_g in the phase P_g. The "signal" is the complex vector H_g with length A_g and phase P_g and the "noise" is measured by the length of the vector n_g and has random phase: (**a**) conditions of high signal to noise; (**b**) conditions of low signal to noise.

$$\frac{\Delta u_g}{d_g} \simeq \frac{1}{2\pi}\left|\frac{noise}{signal}\right| \qquad (27)$$

where the degree of noise is the modulus of $n_g(\bar{r})$ and the signal is measured as the amplitude $A_g(\bar{r})$. It has been shown using simulations that the error in measuring atomic column positions from high resolution images of crystals increases with the square root of the thickness of an amorphous layer covering the specimen [19]. We are now in the position to offer an explanation. The contrast of an image of an amorphous material, measured by the standard deviation of the image intensities, increases approximately with the square root of the thickness following simple arguments from random statistics. For a constant thickness of crystal the signal to noise ratio will also follow this progression and hence the error, given by Equation (27).

A schematic representation of the limiting case where the noise is almost as great as the signal is given in Figure 8b. Here we can see that the amplitude is much more affected by the presence of noise than the phase. We can estimate from the geometry of the figure that the maximum errors will be:

$$\Delta A_g(\vec{r}) \simeq 100\% \qquad (28)$$

$$\Delta P_g(\vec{r}) \simeq \pm\frac{1}{4}\pi \qquad (29)$$

$$\Delta u_g \simeq \pm\frac{1}{8}d_g \qquad (30)$$

To illustrate these points, Figure 9 shows two experimental images, one where the level of noise is fairly weak and the other where the noise is strong. The first image (Fig. 9a) is of a uniform crystal of aluminum (courtesy of Uli Dahmen). The noise to signal ratio was estimated as 0.3 which corresponds well to the standard deviation of 0.26 measured from the amplitude image, Figure 9c, and of 0.33 measured from the phase image, Figure 9e. The second example is a Bragg filtered image of a nanocrystal of CdS_xSe_{1-x} in an amorphous matrix (Fig. 9b). The crystal is barely visible in the amplitude image (Fig. 9d) but clearly visible as an area of uniform phase in the phase image (Fig. 9f) thus illustrating the robustness of the phase to the presence of noise.

The other aspect which affects the measurement of the position of lattice fringes is the mask used in Fourier space to produce the phase images. The size of the mask determines the lateral resolution, or rather, the averaging carried out in real space. For a mask of the size of one Brillouin zone the averaging is effectively carried out over one unit cell. Interpreting the phase on a finer scale is therefore without sense.

Measurement of atomic plane positions

How closely lattice fringe positions correspond to atomic plane positions is a more complicated question to answer and the problems involved are specific to high resolution electron microscopy. To begin with we shall consider slowly varying displacement fields (slow with respect to the size of the unit cell). If the crystal is exactly on a zone axis and the microscope is perfectly aligned the position of the lattice fringes will follow exactly the atomic plane positions. All that might change is that the phases will all shift by exactly π where the contrast inverts due to a variation in the thickness or defocus. These circumstances allow us to interpret the phase images directly in terms of displacement fields in the specimen. The degree to which these conditions apply determines the accuracy of the measurements. In this paper, the examples given satisfy these conditions to a good approximation, or at least sufficiently for the purposes to which the phase images were used. A more detailed analysis requires the consideration of the following aspects:

- projector lens distortions;
- varying microscope misalignments;
- defocus variations linked with misalignements;
- thickness or composition variations linked with misalignments;
- thickness variations linked with crystal tilt.

The image on the screen is a magnified but distorted version of the image formed by the objective lens. Fortunately, the distortions introduced by the projector lenses are relatively small ≈1% change in the magnification across the negative) and are stable [5]. The latter allows the taking of calibration images of, for example, a perfect crystal and subsequent correction of the phase images. Lattice parameters can be measured to an accuracy of ±0.4% with careful calibration [4].

Beam tilt or astigmatism moves lattice fringes with respect to the atomic planes by the introduction of phase shifts [23]. If the thickness, defocus and composition do not change across the image, these phase shifts will be constant and will not affect the measurement of the displacement fields. Beam tilt can, however, vary across the image and is very difficult to calibrate and detect. It is therefore very important to try and limit its effect by, for example, spreading out the beam as large as possible when taking the images. Experiments need to be carried out using a perfect crystal to study the limits in accuracy.

For large beam tilts the phase shifts vary with defocus, so if the exit surface is tilted, the positions of fringes will move even for a perfect crystal. Variations in the thickness and composition will not automatically cause a problem. For linear interference involving only one set of equally strong $\pm\bar{g}$ beams, the phase shift introduced by the misalignments should be independent of the thickness or composition. Variations are introduced when lattice fringes are produced by multiple interference, whether non-linear or linear. The phase shifts will be different for the different beams and therefore as the relative strengths vary the resultant phase shift will be different.

The most common occurrence is probably a combination of thickness variations and crystal tilt. The positions of lattice fringes will vary simply from geometrical considerations and this can even be used to measure the thickness of the specimen for a known constant crystal tilt. This effect is problematic because, as with the variations in the misalignments, it is difficult to detect.

A rapidly changing displacement field will not be faithfully reproduced in the image and lattice fringes will shift due to rapid changes in thickness and composition. This is primarily because the point spread function of the

Figure 9 (*on facing page*). Examples of amplitude and phase images in the presence of noise: (**a**) HREM image of aluminum (courtesy of Uli Dahmen) with high signal to noise; (**b**) 012 Bragg filtered HREM image of a nanocrystal of CdS_xSe_{1-x} in an amorphous matrix (courtesy of Madeleine Gandais) with low signal to noise; (**c**) amplitude image of 111 fringes in aluminum, $A_{111}(\bar{r})$; (**d**) amplitude image of 012 fringes in CdS_xSe_{1-x}, $A_{012}(\bar{r})$; (**e**) 111 phase image, $P_{111}(\bar{r})$, standard deviation noise to signal ratio; (**f**) 012 phase image, $P_{012}(\bar{r})$, area of constant phase reveals nanocrystal.

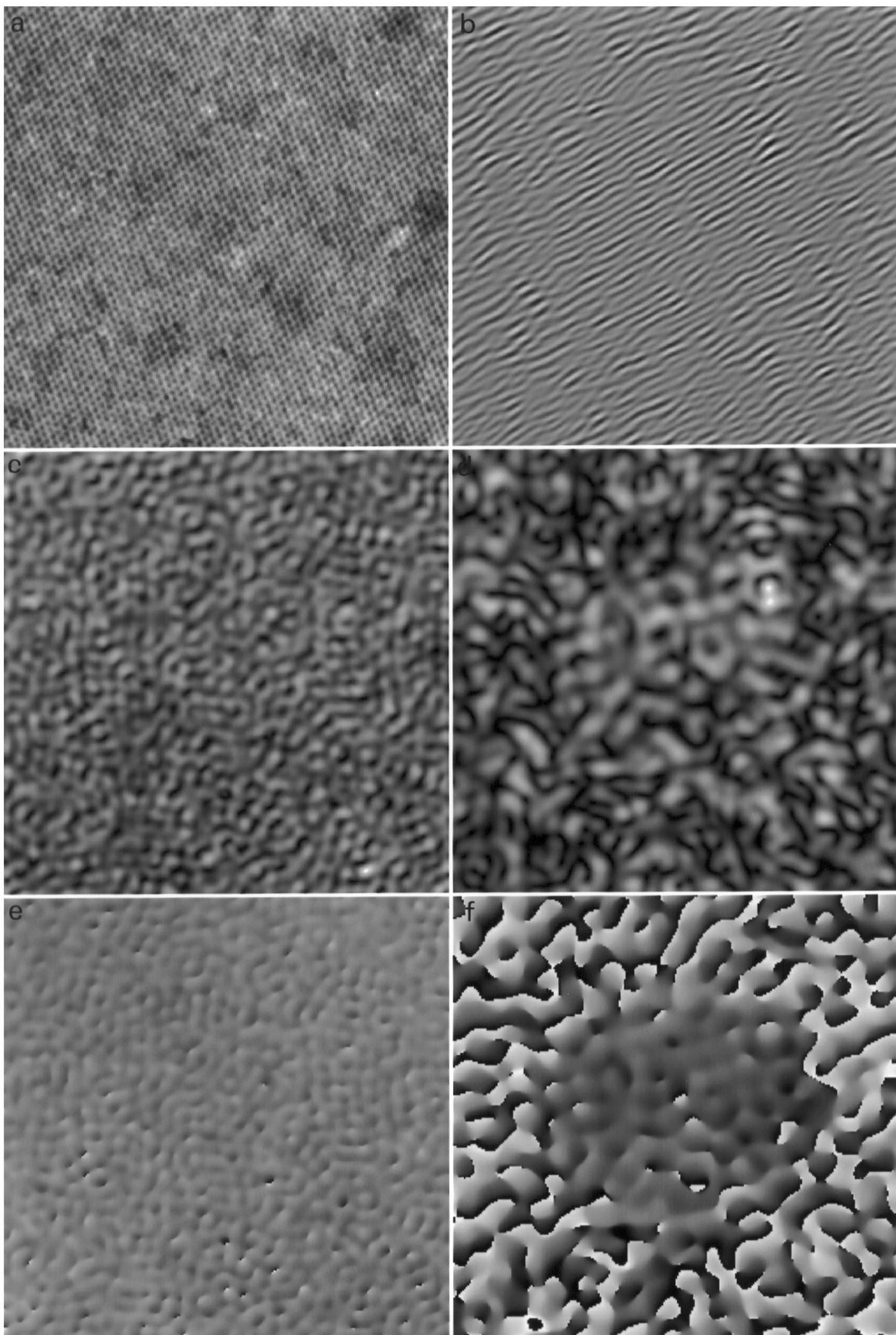
a
b
c
d
e
f

objective lens has a certain width (for both amplitude and phase) but also because of dynamical diffraction and dispersion of the electron wave within the specimen. It is these effects which limit the lateral resolution of the method more than the size of the mask used in reciprocal space. To be more precise, it is the lateral resolution of the simple interpretation of the phase images which is affected. However, there is no reason why simulations cannot be carried out and compared with the experimental results. Indeed, the phase images are much more suitable for comparisons than the original image with its complex intensity distribution. The phase images are also much more closely related to the desired quantity – the displacement field – and therefore the estimations of accuracy are much easier to estimate. Consider, for example, the comparison of high resolution images with simulations by the use of cross-correlation coefficients and then trying to relate the results to structure [15].

Conclusions

It has been shown how variations from an ideal structure can be analysed using geometric phase images. The phase images determine directly the displacement of the lattice fringes and can be used to measure the local reciprocal lattice vector. Under certain circumstances the positions of the lattice fringes are a good approximation to the positions of the atomic planes. The greatest inaccuracies occur for either short-range structural variations, due to dynamical scattering and lens aberrations, or for long-range variations, due notably to combinations of misalignments and thickness variations. The examples shown were interpreted at a medium resolution, on a scale greater than a few lattice planes but much smaller than the area covered by the negative. The important point is that the use of the phase images is not restricted to the regime where the interpretation is simplest. Simulations of phase images can be carried out to determine the accuracy of the measurement of the displacement fields and if necessary compared directly with the experimental phase images. Such comparisons are much more straight forward than comparisons of the original image with simulations. The value of the phase images lie in the fact that they can be used both qualitatively, to reveal important details of the image such as dislocations, lattice rotations, or translation domains, and quantitatively, to make measurements of variations in the structure such as transformation matrices, Burgers vectors, or rigid body displacements.

Acknowledgements

The author is indebted to Laurence Potez, Jean-Luc Putaux, Uli Dahmen and Madeleine Gandais for the experimental results presented in this paper and for numerous collaborations. It is also a pleasure to thank Jean-Pierre Chevalier for useful discussions and for the use of the laboratory facilities at Vitry.

References

[1] Bayle P, Deutsch T, Gilles B, Lançon F, Marty A, Thibault J (1994) Quantitative analysis of the deformation and chemical profiles of strained multilayers. Ultramicroscopy **56**: 94–107.

[2] Bierwolf R, Hohenstein H, Philipp F, Brandt O, Crook GE, Ploog K (1993) Direct measurement of local lattice distortions in strained layer structures by HREM. Ultramicroscopy **49**: 273-285.

[3] Buckett MI, Merkle KL (1994) Determination of grain boundary volume expansion by HREM. Ultramicroscopy **56**: 71–78.

[4] De Ruijter WJ, Sharma R, McCartney MR, Smith DJ (1995) Measurement of lattice-fringe vectors from digital HREM images: experimental precision. Ultramicroscopy **57**: 409–422.

[5] De Ruijter WJ, Weiss JK (1993) Detection limits in quantitative off-axis electron holography. Ultramicroscopy **50**: 269–283.

[6] Friedel J (1967) Solid State Physics, Volume 3: Dislocations. Pergamon Student Editions, Paris.

[7] Hetherington CJD, Dahmen U (1992) An optical moiré technique for the analysis of displacements in lattice images. Scanning Microscopy Suppl **6**: 405–414.

[8] Hirsch PB, Howie A, Whelan MJ (1960) A kinematical theory of diffraction contrast of electron transmission microscope images of dislocations and other effects. Philos Trans Roy Soc London **A252**: 499-509.

[9] Hÿtch MJ (1997) Analysis of variations in structure from high resolution electron microscope images by combining real space and Fourier space information. Microsc Microanal Microstruct, **8**: 41–57.

[10] Hÿtch MJ, Bayle P (1994) Analysis of the variation of individual image periodicities across a strained metal multilayer. In: Proc. 13th International Conference on Electron Microscopy. Editions de Physique, Les Ulis. Vol. 2, pp 129–130.

[11] H_tch MJ, Dahmen U (1996) Measurement of displacements at defects in Al grain boundaries by holographic reconstruction of geometric phase. In: Proc XIth Eur Conf Electron Microsc. Committee Eur Soc Microscopy, Brussels. Vol 1, pp 388-389.

[12] Hÿtch MJ, Gandais M (1995) Quantitative criteria for the detection and characterisation of nanocrystals from HREM images. Phil Mag A **72**: 619–634.

[13] Hÿtch MJ, Potez L (1997) Geometric phase analysis of high resolution electron microscope images of

antiphase domains: example Cu_3Au. Phil Mag A **76**: 1119–1138.

[14] Hÿtch MJ, Stobbs WM (1994) Quantitative criteria for the matching of simulations with experimental HREM images. Microsc Microanal Microstruct **5**: 133–151.

[15] H_tch MJ, Redlich P, Ajayan PM (1996) Quantitative structural analysis of carbon nanotubes by high resolution electron microscopy. In: Proc XIth Eur Conf Electron Microsc. Committee Eur Soc Microscopy, Brussels. Vol 2, pp 417-418.

[16] Jouneau PH, Tardot A, Feuillet B, Mariette H, Cibert J (1994) Strain mapping of ultrathin epitaxial ZnTe and MnTe layers embedded in CdTe. J Appl Phys **75**: 7310–7316.

[17] Lichte H (1992) Holography – just another method of image processing? Scanning Microscopy Suppl **6**: 433–440.

[18] Matthews JW, Stobbs WM (1977) Measurement of the lattice displacement across a coincidence grain boundary. Phil Mag **36**: 373–383.

[19] Paciornik S, Kilaas R, Dahmen U (1993) Assessment of specimen noise in HREM images of simple structures. Ultramicroscopy **50**: 255–262.

[20] Potez L, Loiseau A (1994) High resolution electron microscopy studies of antiphase boundaries in Cu_3Au. Interface Science **2**: 91-103.

[21] Saxton WO, Pitt TJ, Horner M (1979) Digital image processing: the Semper system. Ultramicroscopy **4**: 343–354.

[22] Scheerschmidt K, Knoll F (1994) Retrieval of object information from electron diffraction: theoretical preliminaries. Phys Stat Sol (a) **146**: 491–502.

[23] Smith DJ, Saxton WO, O'Keefe MA, Woods GJ, Stobbs WM (1983) The importance of beam alignment and crystal tilt in high-resolution electron microscopy. Ultramicroscopy **11**: 263-282.

[24] Völkl E, Allard LF, Datye A, Frost B (1995) Advanced electron holography: a new algorithm for image processing and a standardized quality test for the FEG electron microscope. Ultramicroscopy **58**: 97-103.

[25] Wood GJ, Stobbs WM, Smith DJ (1984) Methods for the measurement of rigid body displacements at edge-on boundaries using high resolution electron microscopy. Phil Mag A **50**: 375–391.

Discussion with Reviewers

K. Scheerschmidt: Will you please briefly characterize the difference between your method and Bragg filtering widely applied. Is the difference characterized by the interpretation of the phase as geometrical phase and the resulting conclusions?

Author: There are two aspects which are important both from a qualitative and a quantitative point of view. To begin with, there is a difference between Bragg filtering by placing masks around all of the significant spots, and looking at each of the lattice fringes in turn (the images which I call $B_g(\bar{r})$). Multiple Bragg filtering is just a method of cleaning up the image by removing some of the noise, and is almost cosmetic. Looking at the individual lattice fringes, however, reveals such things as dislocations with the undisturbed $B_g(\bar{r})$ images showing the condition $\bar{g}.\bar{b} = 0$. It may also be possible to see rotations more clearly. Thus qualitatively much of the features seen in phase images can be read from individual Bragg filtering ($B_g(\bar{r})$). However, measurement is best carried out with the phase images -rotations via $\Delta\bar{g}$, Burgers vectors via $\bar{g}.\bar{b} = n/3$, etc.

K. Scheerschmidt: There is a significant difference between the object wave phase and the "geometrical phase", which, in principle, characterizes solely the lattice fringe shift because of the always simultaneous recording of $+\bar{g}$ and $-\bar{g}$ reflections in HREM images. Therefore the displacement field and the change of lattice spacing can directly be interpreted as displacements and bending of the object on only very restricting assumptions, e.g. avoiding multiple scattering and assuming very thin objects. In this simplification, however, the argument of the Burgers circuit holds good for both the displacement and the geometric phase. But can this be demonstrated in general as proposed by your Equations (23) and (24).

Author: The conditions for the simple interpretation of the phase images is not as restrictive as you suggest. For the cases studies here, the underlying assumption is that all the atoms in a particular column are displaced simultaneously (i.e., there is no variation of the displacement field over the foil thickness). Under such circumstances, there are strong reasons to suppose that the wavefunction emerging from the crystal will be peaked at the real atomic column positions. (See for example, the work on electron channeling (see e.g., [26]), or the justifications for the interpretation of high angle dark field images). Dynamical scattering will greatly affect the intensities but is much less likely to shift the apparent column positions. For rapid lateral variations (<1 nm) this approximation will break down, but simulations would have to be carried out in any case given the effect of the objective lens at this resolution. Nevertheless, more work has to be carried out to define the lateral resolution to which the phase images can be reliably interpreted. For the point concerning the Burgers circuit, I think it could be shown generally. The integration around a closed loop must be zero in the absence of point discontinuities. Only under very special circumstances would the thickness of the specimen have a point discontinuity (a ledge or thickness contour would give a line discontinuity). The same would apply to bend

contours.

K. Scheerschmidt: Due to the elastic far field the information of extended defects is located closely around the reflections. May this be the reason that Bragg filtering yields much better results than expected by considering non-overlapping Brillouin zones?
Author: Information at medium resolution (between 1 and 20 nm) is, as you say, located around the Bragg reflections and is therefore directly available in the amplitude and phase images. The information has always been present in the HREM images but has been largely unexploited (because of problems with extracting the information). There are many problems for which the important variations in structure occur over these length scales. For certain cases, *all* of the information is contained in one Brillioun zone, no matter the resolution limit. Compositional variations occurring on a fixed lattice is an example. This is not strictly true for distortions of a lattice but it is reasonable to assume that the majority of the information resides in one Brillouin zone.

N. Bonnet: I appreciate very much this work and consider that the way the Fourier phase is exploited for obtaining information (lattice distortion, ...) in the real space is very innovative. It was recognized for a long time that the amplitude spectrum contained only a part of the total information, but few attempts were made for exploiting the phase spectrum. Do you think this original approach could be extended (with necessary variations) to non-periodic objects?
Author: The phase method works especially well when analysing variations which can be described as a modulation of a set of fringes, i.e., where the local reciprocal lattice vector does not differ greatly from the average lattice vector $\vec{g}$. Analysing non-periodic objects such as grain boundaries is therefore possible if there are common Bragg reflections. I am currently working on ways of analysing interfaces where the Bragg reflections are not continuous. Another type of non-periodic object which has been treated is a nanocrystal (see [12]). However, if by non-periodic objects you mean "ordinary" images with no obvious lattice fringes, there is no immediate way that I can see of extending the method though it may, as you suggest, give interesting results.

N. Bonnet: I would like to address some questions of terminology. First, I think it should be stated that the method you use (and which you call "single side-band holographic reconstruction") can be related to what is called "Gabor filtering" in the image processing community. The aim of Gabor filters (Gaussians modulated by sines and cosines in the real space) is precisely to obtain the local amplitudes and phases (at the given central frequency of a band-pass filter). In this context, you write (in "Measurements of fringe positions") that the size of the mask determines the resolution. What about the shape of the mask? Did you try to see if any difference occurs when replacing the disc-shaped mask by a Gaussian mask (Gabor filter)?
Author: The method can, indeed, be related to Gabor filtering where the creation of local images of $H_g'(\vec{r})$ are a special case. Following your suggestion I have included a short section in a later paper on the phase method [9]. Also in that paper, Gaussian shaped masks were experimented with having a standard deviation of g/4. Qualitatively, the noise is reduced by using Gaussian filters and there are less spurious fringes. The lateral resolution of the images has, however, been reduced. The important point is that for quantitative results at lateral resolutions of less than 1 nm the results must, in any case, be compared with simulations. The shape of the mask does not then matter if an identical mask is used for both the experimental and simulated images.

Additional Reference

[26] Van Dyck D, Op de Beeck, M (1992) Direct methods in high resolution electron microscopy. Scanning Microscopy Suppl **6**: 115–120.